

3 Design and Construction of a Cherenkov Detector for 4 Compton Polarimetry at the ILC

5 Christoph Bartels^{1,2}, Joachim Ebert², Anthony Hartin¹,
6 Christian Helebrant¹, Daniela Käfer¹, and Jenny List¹

7 1- Deutsches Elektronen-Synchrotron DESY
8 Notkestr. 85, 22607 Hamburg, Germany

9 2- Universität Hamburg, Institut für Experimentalphysik
10 Luruper Chaussee 149, 22761 Hamburg, Germany

11 Abstract

12 This paper describes the design and construction of a Cherenkov detector con-
13 ceived with regard to high energy Compton polarimeters for the International Linear
14 Collider, where beam diagnostic systems of unprecedented precision must comple-
15 ment the interaction region detectors to pursue an ambitious physics programme.
16 Besides the design of a prototype Cherenkov detector, detailed simulation studies
17 are presented. Results of a first testbeam campaign with the main objective of
18 validating the simulation in terms of the light distribution inside the channels and
19 the channel response are presented. Furthermore, a new method for aligning the
20 detector without the need of dedicated data taking has been developped.

21 Submitted to JINST

1 Introduction

The measurement and control of beam parameters to permille level precision will play an important role in the physics programme [1, 2] of the International Linear Collider (ILC). For electroweak processes, the absolute normalisation of expected event rates depends on both, luminosity and polarisation. The luminosity will be measured to a precision of 10^{-3} to 10^{-4} , while for the luminosity weighted polarisation average an accuracy of 10^{-3} seems achievable [3].

While for beam energy and luminosity measurements the ILC's precision goals have already been achieved at previous colliders, polarimetry has to be improved by at least a factor of two compared to the most precise previous measurement of the SLD polarimeter [4].

The polarisation determination at the ILC will combine the measurements of two dedicated Compton polarimeters, located upstream and downstream of the e^+e^- interaction point, with measurements from the e^+e^- interactions themselves. While the e^+e^- data will finally yield the absolute polarisation scale, the polarimeters provide fast measurements which allow to track variations over time and to detect possible correlations with the luminosity or the polarisation of the other beam. Therefore, each polarimeter has to reach a systematic accuracy of at least $\delta\mathcal{P}/\mathcal{P} = 0.25\%^1$. Two polarimeters per beam are required in order to measure the polarisation of the beams in collisions. Both polarimeters have been designed for operation at beam energies between 45 GeV and 500 GeV. A detailed description of the polarimeters can be found in [5].

Both polarimeters make use of the polarisation dependence of Compton scattering to ensure a non-destructive measurement of the longitudinal beam polarisation. Circularly polarised laser light is shot under a small angle onto the individual bunches causing typically in the order of 10^3 electrons² per bunch to undergo Compton scattering. The energy spectrum of these scattered particles depends on the product of laser and beam polarisations, so that the differential rate asymmetry with respect to the laser helicity is directly proportional to the beam polarisation. Since the scattering angle in the laboratory frame is less than $10\text{ }\mu\text{rad}$, a magnetic chicane is used to transform the energy spectrum into a spatial distribution which is then measured by Cherenkov detectors.

A Cherenkov detector was chosen for several reasons:

- (i) In combination with the magnetic chicane, it allows to measure the energy spectrum of many electrons arriving simultaneously. With about 10^3 Compton interactions per electron bunch, a statistical precision of $\delta\mathcal{P} = 1\%$ is achieved for each of the about 3000 bunch positions in a train after only 20 trains ($\hat{=}$ 4 seconds). For the average polarisation of all bunch positions, this corresponds to a statistical error below 0.1% after 1 second [5].
- (ii) For relativistic electrons ($\beta = v/c \approx 1$), Cherenkov radiation is independent of the electron energy. Thus, the number of Cherenkov photons will be directly proportional to the number of electrons per detector channel.

¹for typical ILC beam polarisation values of $\mathcal{P}_{e^-} \geq 80\%$ and $\mathcal{P}_{e^+} \geq 30\%$ or even $\geq 60\%$

²or positrons in case of the positron beam of the ILC which is equipped analogously.

(iii) Typical Cherenkov media like gases or quartz are sufficiently radiation hard to withstand the flux of 10^7 electrons passing through the detector per second.

Developing a Cherenkov detector suitable for achieving the target precision of $\delta\mathcal{P}/\mathcal{P} = 0.25\%$ demands improvements in various areas of the experimental setup. On the detector side, especially the linearity of the detector response, its homogeneity with respect to the entrance point of the Compton electrons as well as the detector's alignment to the beam axis are important to control. In order to test these and further aspects, a prototype detector has been designed, simulated and constructed as described in the chapters 2 and 3. The prototype has been operated in a testbeam campaign at the ELSA stretcher ring in Bonn, with the main objective of validating the simulation in terms of the channel acceptance and light distribution inside the channels employing multi-anode photomultipliers. The results of these studies are presented in chapter 4, including a new method for aligning the detector directly from polarimetry data without the need of expensive dedicated alignment data taking.

2 Detector Design and Simulation

A conceptual design for the Cherenkov detector envisioned for the ILC polarimeters is shown in Figure 1(a). It will consist of staggered ‘U-shaped’ aluminium channels lining the tapered exit window of the beam pipe, similar to the design proposed in [6]. The channels are filled with a Cherenkov gas so that relativistic electrons traversing their base emit Cherenkov radiation which is reflected upwards in the hind U-leg to the photodetectors. A single channel is sketched in Figure 1(b).

The wavelength spectrum of Cherenkov radiation is given by:

$$\frac{dN^\gamma}{d\lambda} = 2\pi\alpha \left(1 - \frac{1}{n^2\beta^2}\right) \frac{1}{\lambda^2} \ell, \quad \text{with:} \quad \begin{array}{ll} N^\gamma & : \text{mean number of photons,} \\ \lambda & : \text{wavelength,} \\ \alpha & : \text{fine structure constant,} \\ n & : \text{radiator's refractive index,} \\ \beta & : \text{velocity } (\beta = \frac{v}{c}), \\ \ell & : \text{radiator length} \end{array} \quad (1)$$

While the velocity (β) can be regarded as constant for electron energies relevant at the ILC, the refractive index depends on the wavelength, as well as on the temperature and the gas pressure. At small wavelengths, the refractive index typically rises like $(n-1) = A/[\lambda_0^{-2} - \lambda^{-2}]$. This behaviour has been measured for C_4F_{10} for the Ring Imaging Cherenkov Detector of the DELPHI experiment at LEP [7]. Furthermore, $n-1$ is proportional to the number density of molecules for $n \approx 1$ [8] and thus increases proportionally with the inverse temperature and the pressure.

To simplify further references, a right-handed coordinate system, as shown in Figure 1, will be used throughout the rest of this publication. Assuming the electron beam travels in positive z -direction, the y -axis points upwards, and the x -axis to the left when looking in the direction of the electron beam.

2.1 Requirements and conceptual design

The design of the Cherenkov detectors for the ILC polarimeters is driven by the requirements listed in the following. In most cases, the exact values will depend on the final design of the accelerator, of the magnetic chicane and of the laser system, which is still subject to change. Therefore only indicative numbers are given here.

Dynamic Range

The detector has to be able to cover a dynamic range from $\mathcal{O}(1)$ to several hundreds of Compton electrons per channel and bunch crossing. This applies especially to the channels near the Compton edge, where the asymmetry with respect to the laser helicity is largest [5].

Homogeneous detector response

At the SLD polarimeter, variations of the detector response with respect to the electrons' entry positions lead to a correction on the analyzing power in the order of $1\% \pm 0.5\%$ [9]. Although part of this effect was due to a preradiator, which is not foreseen to be employed at the ILC, the SLD example shows that the homogeneity of the detector response needs to be considered and should not contribute more than a permille to the total uncertainty budget.

Alignment

The Compton edge position has to be controlled to $\mathcal{O}(100 \mu\text{m})$ in order to keep the impact on the analyzing power below 0.1%. Tilts of the detector typically result in changes of the analyzing power in the order of 0.05%/mrad, depending on the considered channel and rotation axis. These numbers are similar to those observed at the SLD polarimeter [9]. At SLD the alignment was monitored regularly in a dedicated operation mode by moving the detector with respect to the beam and interpolated in between these calibration runs. While this approach could be followed at the ILC, it costs expensive accelerator operation time for which no polarisation measurement can be provided. Therefore the development and test of alignment methods which can be performed during polarimetry data taking are among the goals of the prototype presented here.

Robustness with respect to backgrounds

A gas with a Cherenkov threshold in the MeV-regime should be used to avoid the emission of Cherenkov light from low energetic electrons and muons, e.g. from the beam halo, from beam-gas interactions, or electrons pair-produced from synchrotron radiation. A layout allowing the photodetectors and electronics to be placed well outside the beam-plane is mandatory.

Detector Linearity & Calibration system

The linearity of the detector response has to be controlled to a level of about 0.75% in order to limit the effect on the analyzing power to 0.1%. Therefore, a dedicated calibration system is foreseen to monitor the detector response, especially its linearity, in-situ. This could be realised by equipping the channels with light emitting diodes (LEDs) which should also be placed outside the beam-plane. Such a system could collect data during breaks in the accelerator operation, or even in-between two ILC bunch trains.

The chosen channel geometry is illustrated in Figure 1. The (Compton scattered) electrons traverse the horizontal U-base, while the upward pointing legs serve to place the photodetectors and the calibration system outside of the beam-plane. With increasing length of the U-base more Cherenkov light is produced, but on the other hand the alignment requirements become more stringent and additional reflections will decrease the light yield. Simulations suggest that a length of 15 cm is a reasonable choice.

In contrast to the ILC-like design of 20 staggered channels (c.f. Figure 1(a)), the prototype detector consists of two parallel, non-staggered channels. Apart from this difference, the prototype detector allows to test all relevant aspects of the full detector. Especially it will serve in the future as a test bed for the calibration system which is currently under development as well as for the final choice of photodetectors.

2.2 Optical simulation

A detailed simulation of the prototype detector based on GEANT4 [10] has been created in order to support the design process and the interpretation of the testbeam data.

For electrons and positrons Cherenkov radiation, multiple scattering, ionisation, bremsstrahlung and annihilation are simulated. Apart from annihilation, the same processes are taken into account for muons, which are relevant when studying the impact of accelerator background. For the Cherenkov photons optical processes have to be considered since their wavelengths are much larger than a typical atomic spacing. In particular, absorption in the photodetector entrance window, boundary effects (like reflection and absorption) at the channel walls, as well as Rayleigh elastic scattering have been included in the simulation [11].

As Cherenkov gas, perfluorobutane (C_4F_{10}) has been chosen due to its high threshold of 10 MeV, which makes the detector robust against background from low energetic charged particles. The wavelength dependence of the refractive index is implemented in the simulation according to [7]. Since the polarisation measurement is based on rate asymmetries, it will be insensitive to the exact value of n . Also variations of n with time which are slow with respect to the laser helicity flipping rate (like thermal variations) will cancel out within the asymmetry. Therefore such effects are currently not simulated and the temperature and gas pressure inside the detector box are set to $T = 20^\circ\text{C}$ and $p = 1\text{ atm} = 1.01325\text{ bar}$, respectively.

Pure C_4F_{10} is fully transparent even in the far UV range. In the presence of impurities, especially water or oxygen, the transparency can drop significantly for wavelengths smaller than 200 nm [12], where two of the four employed photodetectors are sensitive, c.f. Section 3.1. Since the precise knowledge of the absolute photon yield is not crucial for the rate asymmetry measurement, gas impurities have not been implemented in the simulation.

Two different types of aluminium have been implemented in the simulation according to the reflectivity studies summarised in Section 2.5. Three of the four walls of each channel are made of diamond-milled aluminium, while the inter-channel wall consists

of two 150 μm sheets of rolled aluminium. The wavelength dependency is interpolated linearly between the values listed in Table 1. While for the diamond-milled walls the absolute normalisation is fixed to the values in Table 1, the reflectivity of the rolled sheets can be adjusted via the ratio of the two materials' reflectivities $r := R_{\text{roll}}^{\text{eff}}/R_{\text{diam}}$, which is a parameter of the simulation.

Figure 2 shows the channel structure with a single electron (red line) passing from left to right through the U-base of the right-hand side channel. It emits Cherenkov light (green), which is reflected upwards at the end of the U-base towards the photodetector. Cherenkov light produced outside the channel structure in the ambient gas cannot reach the photodetectors. The optical simulation ends at the photocathode and all Cherenkov spectra are stored for further processing and digitisation.

Unless specified otherwise, the simulations shown in the following sections were performed in view of the testbeam situation at ELSA with a two-dimensional Gaussian with standard deviations $\sigma_x = \sigma_y = 0.5\text{mm}$ as beam profile and zero divergence over the length of the detector prototype. Per beam position, 10^6 electrons with an energy of 2 GeV have been simulated.

2.3 Cherenkov spectra and light distributions

The number of emitted Cherenkov photons follows a Poisson distribution with the mean value N^γ given by the integral of Formula 1 over the relevant wavelength range. The number of photons reaching the photocathode is expected to follow a Poisson distribution as well, as long as other contributions, for instance from electrons showering in the channel walls or multiple-scattering in the entrance window, are small.

To study the influence of the detector geometry and the reduced reflectivity of the inter-channel wall on the expected light distribution, the simulation has been run twice with different reflectivities for the inter-channel wall and the beam centered on one of the two channels.

Figure 3 shows the number of Cherenkov photons reaching the photocathode for both cases: In Figure 3(a), all channel walls have been simulated with the reflectivity of diamond-milled aluminium, resulting in on average $N^\gamma = 68$ photons per 2 GeV electron. When the reflectivity of the inter-channel wall is reduced to $r = 50\%$, about 16% less photons reach the photocathode, so that the average decreases to $N^\gamma = 57$ photons as shown in Figure 3(b).

In both cases, the distributions of the number of photons reaching the photocathode is not exactly Poissonian, but exhibit a small Gaussian broadening due to multiple scattering in the entrance window. For illustration, both a pure Poissonian (labeled P) as well as a Poisson convoluted with a Gaussian (labeled $P \otimes G$) have been fitted to the distributions. The respective χ^2 per degree of freedom values clearly prefer the convoluted fit over the pure Poissonian. But with $\sigma_{\text{Gauss}} \approx 2$ photons, the broadening is small compared to the mean number of photons for both reflectivity scenarios and is expected to be negligible for the much higher electron energies relevant in the polarisation measurement.

Figure 4 shows the wavelength spectrum of these photons obtained from the simulation with the reduced reflectivity for the inter-channel wall. Figure 4(a) illustrates the distribution at the photocathode, showing the expected $1/\lambda^2$ wavelength dependence for Cherenkov radiation. It is cut off below $\lambda_{\text{low}} = 160$ nm and above $\lambda_{\text{high}} = 900$ nm in the simulation since the photodetectors are not sensitive outside this wavelength range. Figure 4(b) shows the wavelength spectrum after convolution with the quantum efficiency of the 2×2 multi-anode photodetector (HAMAMATSU R7600U-03-M4). This quantum efficiency is shown in the insert in Figure 4(a) [13]. On average, 6.5 photons are detected corresponding to the integral of the histogram in Figure 4(b).

Figure 5 shows the resulting spatial light distributions on the photocathode, again for two different assumptions on the reflectivity of the inter-channel wall. The result obtained with equal reflectivities for all inner surfaces is illustrated in Figure 5(a). In this case, the observed non-uniformities are due to the influence of the detector geometry. For reference a white dot indicates the position of the channel centre. The distribution exhibits an X-like structure of increased photon yield which is symmetrical about the x - and z -axes. A reduced light yield is visible in two narrow bands at $z = \pm 1$ mm as residuals from the 90° reflection at the end of the Cherenkov section. Lowering the reflectivity of the inter-channel wall (located at $x = -4.25$ mm) changes the symmetry of the light pattern as shown in Figure 5(b). Near the inter-channel wall, the light yield is reduced, but the X-like structure remains.

These features can be understood with the sketches in Figure 6, which illustrate two cases of photocathode illumination for an electron traversing the channel along its central axis and assuming the Cherenkov angle of the chosen gas ($\Theta_{\text{Ch}} = 3^\circ$). Photons emitted in the horizontal (or vertical) plane illuminate the entire width of the channel at the photocathode as shown in Figure 6(a). Due to the larger effective channel cross section, photons emitted towards the corners illuminate only half the channel width at the photocathode as illustrated in Figure 6(b). This leads to a higher photon yield near the diagonals of the channel cross section which also explains the X-like structure observed in Figure 5. In addition, Figure 6(b) explains the fact that the lower reflectivity of the inter-channel wall leads to a depletion on the same side of the channel.

2.4 Yield asymmetries and beam position

The light distribution on the photocathode has been simulated for a grid scan of 4×4 beam positions with 10^5 electrons per position, assuming equal reflectivities for all channel walls. Figure 7(a) depicts the light yield on the photocathode for electrons entering the Cherenkov section at a fixed y -position and four different x -positions. The y -position of the beam, indicated by the white dots in Figure 7(a), translates directly to the z -position in the readout plane of the photodetector. A clear correlation between the light pattern and the beam position can be observed in these simulations. If this correlation persists in real data, it could potentially be a very useful tool both in a testbeam experiment for tuning the simulation and studying the detector properties in detail, as well as in the final polarimeter for monitoring the alignment and the Compton edge position during data-taking without the need for expensive dedicated calibration beam time.

In order to pursue this idea further, the light pattern is quantified in terms of the asymmetries in Figures 7(b,c), which are calculated from the light intensities for scans in the x - and z -directions, respectively. For each beam position the corresponding asymmetries are defined as

$$A_x = \frac{I_x^+ - I_x^-}{I_x^+ + I_x^-} \quad \text{and} \quad A_z = \frac{I_z^+ - I_z^-}{I_z^+ + I_z^-} ,$$

where I_x^+ (I_z^+) corresponds to the intensity in the right (upper) half of a channel and I_x^- (I_z^-) to the intensity in the left (lower) half, respectively.

These asymmetries have an approximately linear dependence on the beam position.

Figure 7(b) shows a slight variation of the slope of A_x depending on the y position of the beam, while in Figure 7(c) the same A_z is observed for all x positions. This behavior is expected since the active length of the channels increases with y due to the 45° angle of the mirrors.

2.5 Reflectivity measurements

When choosing the detector materials, different qualities of aluminium have been considered, primarily with regard to their reflectivity, but also concerning smoothness and mechanical stability.

Reflectivity measurements of small aluminium probes (blocks, sheets, and sub mm-foils) of different quality have been performed with a modified transmission spectrometer [14]. The path of the measurement beam inside the spectrometer has been changed such that it reflects off four small blocks instead of passing through the probe material, as shown in Figure 8(a). One photomultiplier detects the previously splitted reference and measurement beams and thus provides a measure of how much light is reflected by the four blocks' surfaces with respect to the reference beam.

Figure 8(b) shows measurements of the reflectivity as a function of the wavelength between $\lambda = 160$ nm and 600 nm for diamond-milled aluminium blocks and for a sample of rolled aluminium foil purchased from GOODFELLOW³. In both cases the reflectivity rises at low wavelengths up to $\lambda \approx 250$ nm and is approximately constant at larger wavelengths. For the diamond-milled blocks, the reflectivity reaches $R_{\text{diam}} \approx 85\%$ in the plateau region, which is in good agreement with [15]. This material is employed for the mirrors at the ends of the U-base, where the reflection occurs approximately under 45° as in the spectrometer. Therefore these measured values have been implemented in the simulation.

In case of the rolled foil, the measured plateau value of $R_{\text{roll}} \approx 40\%$ is low, but still in the range of reflectivities observed for not perfectly smooth surfaces [15]. However it is not directly applicable to the situation in the prototype for several reasons: To start with, the

³GOODFELLOW GmbH, Germany; Aluminium foil: AL000601 (thickness: 0.15 mm, purity: 99.0%, hardness: hard)

reflections on the channel walls occur predominantly under shallow angles ($\Theta_{\text{Ch}} = 3^\circ$). Furthermore, any light not following the path expected for an ideal reflector, be it due to a finite size of the specular reflection highlight or due to a diffuse reflection component, will lead to an immediate intensity loss in the spectrometer, while it still has a high probability to reach the photodetector at end of the channel in the prototype. Therefore the absolute scale of the spectrometer measurements is considered as a lower limit for the effective reflectivity of the inter-channel wall. The wavelength dependency observed in the spectrometer measurements is taken into account in the simulation, but the overall ratio $r = R_{\text{roll}}^{\text{eff}}/R_{\text{diam}}$ is a parameter which is varied between 50% and 100% as extreme cases, and which ultimately needs to be determined from prototype data. In particular, it can be determined from the detector response as function of the beam position if enough position scans with sufficient beam quality are available. This is illustrated in Figure 9(a), where simulated beam position scans for different values for r exhibit different slopes of the plateau region towards the inter-channel wall. Figure 9(b) shows measurements of this slope for both detector channels. The different absolute values of the slopes observed for the left and right channel are due to residual misalignment (c.f. Section 4.3). Comparisons with a simulation including the misalignment suggest a realistic value of r of approximately 85%, which was used in further simulations.

3 Construction of the Prototype

The channel dimensions of the prototype were chosen to match the design criteria discussed in section 2.1. The length of the U-base relevant for the emission of Cherenkov radiation from traversing electrons is 150 mm and the height of the two U-legs is 100 mm. A quadratic cross section of $8.5 \times 8.5 \text{ mm}^2$ has been chosen to match the cathode geometry of two square multi-anode photomultipliers. Section 3.1 gives further details of the employed photodetectors and their characteristics.

The size of the outer box is $230 \times 90 \times 150 \text{ mm}^3$ (L×W×H) allowing for easy accommodation of the channel structure. Parts of the technical drawing, e.g. the channel structure and its placement inside the box, are shown in Figure 10.

Perfluorobutane was chosen as Cherenkov gas due to its high Cherenkov threshold of about 10 MeV for electrons. In addition it is neither flammable, nor explosive, contrary to propane or isobutane. The 10 mm thick aluminium lid of the box holds an electronic pressure gauge suited for remote read-out. The entrance and exit windows for the electron beam consist of 0.5 mm thin aluminium sheets.

All mountings for LEDs, photodetectors and windows have been designed to be gas- and light-tight, as well as easily exchangeable.

3.1 Photodetectors and their mountings

The hind U-leg can be equipped with four different types of photodetectors, which are listed in Table 2 along with some of their characteristics. They differ in geometry (square

versus round) and the number of anode pads as illustrated in Figure 11. Their gains are in the order of 10^6 with wavelength thresholds between 160 nm and 300 nm and their response times range from 6.5 ns to 28 ns. In case of the square multi-anode photodetectors (MAPMs), one quadrant of their cathodes exactly matches one detector channel. Thus, both detector channels can be read out simultaneously by the same photodetector.

While the round single-anode photodetectors (SAPMs) are inserted into their respective mountings using appropriate O-ring seals, the MAPMs need to be glued into their mountings. Epoxy resin mixed with black paint was used as glue to ensure gas- and also light-tightness. The mountings themselves were manufactured from poly-oxy-methylene (POM) for electrical insulation. They provide for three different photodetector positions relative to the detector channels as depicted in Figure 12. In addition, both MAPM mountings can be rotated by 180° for systematic studies.

3.2 LED calibration system

The front U-leg of the detector serves for calibration purposes and is equipped with one LED per channel. The LEDs have a peak wavelength of 470 nm (HLMP-CB30-NRG, Agilent Technologies [16]) and are glued into their mounting structure using epoxy resin.

As shown in Figure 13, two slender 18 mm long POM tubes encase the LEDs to ensure that the light from one LED does not enter the neighbouring channel through a small slit in the inter-channel wall necessary for gas circulation. A temperature sensor is placed in between the two POM tubes to allow for temperature monitoring.

The LEDs and the temperature sensor are fixed in a mounting which has been designed to be easily exchangeable, because the prototype will serve in the future as a test bed for a suitable calibration system which is currently under development.

3.3 Additional components

Two small, light-tight boxes protect the MAPMs and their electrical bases. A rotation mechanism on a plastic base plate allows to adjust the detector's horizontal tilt about the y -axis in reproducible steps of 0.125° between $\alpha_y = \pm 3.0^\circ$. The fixed rotational axis lies in the center of the front U-leg as illustrated in Figure 10(b).

4 Beam Tests at the ELSA Accelerator

Beam tests with the prototype detector were performed in an external beam line at ELSA. The ELEktronen-Stretcher-Anlage (ELSA) is an electron accelerator consisting of three stages: injector LINACs, a booster synchrotron and the stretcher ring [17]. A beam of polarised or unpolarised electrons of variable energy up to 3.5 GeV can be stored and used for various experiments in different beam line areas around the storage ring. The stretcher ring has a circumference of 164.4 m corresponding to a time of 548 ns for one revolution. The ELSA beam is structured by the RF frequency of 500 MHz. Of 274 buckets in total, a variable fraction can be filled. As an example, Figure 14 shows the fill structure for four revolutions of 548 ns for a partially filled ELSA accelerator.

4.1 Setup and pedestal stability

During the testbeam period, ELSA was operated in *booster mode* with the electrons being injected at an energy of 1.2 GeV and subsequently accelerated to 2.0 GeV. The machine cycle is 5.1 s with an extraction time of 4.0 s and the beam can be focussed to a spot size of about 1 mm. The extraction current is adjustable from approximately 10 pA to 200 pA leading to respectively 35 to 700 electrons traversing the detector per ELSA revolution. In comparison, up to 250 electrons per bunch crossing are expected in the most populated channel of a polarimeter Cherenkov detector at the ILC.

The beam clock signal was used to provide the gate for the QDC (charge sensitive analog-to-digital converter), as illustrated in the block diagram of the readout chain in Figure 15. The gate width was adjusted between 100 ns and 480 ns to integrate over the filled part of one ELSA revolution.

The detector was filled with the Cherenkov gas C_4F_{10} at a slight overpressure of about 140 mbar. This overpressure remained stable although frequent changes to the setup prevented a monitoring of the gas pressure for continuous time periods longer than two weeks. Figure 16 shows the Cherenkov detector set up in one of the ELSA external beam lines, directly behind a dipole magnet bending the electrons by $\approx 7.5^\circ$ towards a downstream beam dump. The detector was mounted on its base plate (black) and additionally affixed to a stage moveable along the x - and y -axis. The two angles, α_x and α_z , had to be adjusted using a water-level.

The filled grey histogram in Figure 17(a) depicts the QDC response with no bias voltage applied to the photodetector (pedestal) and without ELSA operation, while the open histograms show the QDC response for a bias voltage of 400V applied to the photodetector (dark current). The dark (light) colour corresponds to the case without (with) beam circulating in ELSA. All three histograms are normalised to the same number of entries. Both, the photodetector dark current and the accelerator operation, lead to a slight broadening of the pedestal peak, but its position remains stable. This is illustrated further by Figure 17(b) which shows again a dark current signal (filled grey histogram) recorded while beam was circulating in ELSA, and, in addition, Cherenkov signals for three different extraction currents (open coloured histograms). Besides the beam signals, each open histogram features a small peak coinciding with the pedestal position because the data taking continued during the 1.1 s of filling and acceleration. This provides the opportunity to monitor the pedestal stability continuously during beam operation. The relative areas of beam signal and pedestal peaks reflect the 4:1 ratio defined by the 5.1 s-periodic cycle of extraction and refill/acceleration times. Longterm monitoring showed that the pedestal position remained stable within 1 QDC count, which fulfills the ILC requirements. All following Figures show pedestal-subtracted signals.

4.2 Online alignment and channel response function

The alignment of the detector with respect to the electron beam line was obtained from beam data. By moving the detector stage, the incident beam position on the entrance

window was scanned in horizontal (x) and vertical (y) directions. The adjustment procedure requires one vertical scan for each detector channel and a series of horizontal scans across both channels for different tilt angles α_y , as shown in Figure 18.

When the detector is tilted, the electrons will not have the full channel length to produce Cherenkov light. The maximal signal for any given x position of the beam will be smaller than for a perfectly aligned detector⁴. For each tilt angle, the beam x position resulting in the highest signal is determined as displayed in Figure 18. With this procedure, the best alignment of the detector with respect to the beam line was obtained for a tilt angle of $\alpha_y = 1.33^\circ$ with a very small statistical uncertainty of 0.03° . Due to the step size of the rotation mechanism, this value was approximated to $\alpha_y^0 = 1.35^\circ$ for all following measurements.

Measurements of the detector response as function of the horizontal beam entry position were performed with the single-anode photomultiplier R7400U-06 and with the 2×2 multi-anode photomultiplier (R7600U-03-M4) positioned on the detector channels as illustrated in Figure 12(c). Figure 19(a) shows for the latter case the results of an x -scan across both detector channels. Two Gaussian fits indicate the respective channel centres to be at $x_{\text{right}} = (7.4 \pm 0.1)$ mm and $x_{\text{left}} = (16.4 \pm 0.1)$ mm, leading to a distance of $\Delta x = (9.0 \pm 0.2)$ mm. This agrees with the nominal distance between the channel centres of $\Delta x_{\text{nom}} = 8.8$ mm, given by the width of one channel and the inter-channel wall.

Figure 19(b) shows x -scan data for the single-anode photomultiplier, where a broad plateau is observed. The width of the signal region is determined from two sigmoidal fits to the edges of the plateau. At 50% of the plateau height, this width is found to be $w = (9.4 \pm 0.3)$ mm, where the error is dominated by the table position accuracy. This value is significantly larger than expected from the physical channel width and from Monte-Carlo simulations. Understanding the channel response function to the precision level required for the ILC will need further data with more stable beam conditions than available from the 2009 campaign.

The impact of the beam conditions becomes evident by comparing the observed channel response functions from 19 with the corresponding photographs of a fluorescent screen placed on the detector entrance window: Figure 20(a) shows a very elongated beam spot observed at the time the MAPM data were recorded (Fig. 19(a)), which explains the absence of any plateau in the detector response. The significantly smaller and nearly round beam spot shown in Figure 20(b) was achieved during data taking with the SAPM (Fig. 19(b)).

4.3 Alignment via spatial asymmetries

The anode of the 8×8 multi-anode photomultiplier (R7600-00-M64) is finely segmented with 16 anode pads covering a single Cherenkov channel, thus offering spatial resolution within a detector channel. Since two QDC channels were broken, only six channels were

⁴Due to the channel geometry, this holds for all tilt angles larger than 0.027° .

available to realise the readout configuration illustrated in Figure 21. The numbers indicate the QDC channel utilised to read out the sum signal of either four or eight anode pads of the photodetector.

Figure 22 shows the results of (a) an x -scan across both detector channels and (b) the corresponding y -scan across the left channel. As expected, the signals in QDC channels 2 and 3 are about twice as large as in the other channels since eight instead of only four anode pads are grouped together. The asymmetric response reflects the incident beam position. For each QDC channel, the largest signal is observed when the beam enters on the opposite side of the detector channel. This confirms the prediction of one glancing angle reflection for most of the photons obtained from MC simulations (c.f. Section 2.3 and 2.4).

For a more detailed comparison of the responses of the different anode segments, the same data are displayed again in Figure 23, scaled and mirrored to correct for the two above effects. Possible reasons for the remaining shape and amplitude differences comprise gain variations between the pads and residual detector misalignment.

The vertical beam scan data have been used to calibrate the relative gain variations between the different groups of anodes. After applying these calibrations to the horizontal beam scans, two x -asymmetries, A_x^{lower} and A_x^{upper} , are calculated from the four anode groups QDC 4 to QDC 7 (c.f. Figure 21):

$$A_x^{lower} = \frac{\text{QDC 5} - \text{QDC 4}}{\text{QDC 5} + \text{QDC 4}} \qquad A_x^{upper} = \frac{\text{QDC 6} - \text{QDC 7}}{\text{QDC 6} + \text{QDC 7}}$$

The resulting asymmetries are displayed in Figure 24(a), together with the expectation from simulation assuming residual tilts of $\alpha_x = 0.2^\circ$ and $\alpha_y = -0.2^\circ$ and a reflectivity ratio of $r = 85\%$. The error bars on the data points correspond to the remaining gain differences between the anode pads. Uncertainties which are in common between the different pads cancel out within the asymmetries. The error bands on the simulated curves are obtained by varying α_y by $\pm 0.1^\circ$ in the simulation. A similar variation of α_x has no visible impact on A_x . Figure 24(b) shows A_x^{lower} and A_x^{upper} for the other detector channel, read-out by the neighboring quadrant of the 8×8 MAPM⁵, compared to the simulation using exactly the same parameters as before. The obtained precision of $\pm 0.1^\circ$ is very close to the requirements for the ILC, which shows that in principle the light distribution inside a channel can be understood to sufficient precision. But due to the extremely limited number of datasets with good beam conditions (c.f. Section 4.2) no further independent beam scan is available from the 2009 data-taking period at ELSA. Therefore further data-taking will be needed for conclusive statements on the use of multi-anode photodetectors in ILC polarimeters.

⁵Due to the two broken QDC channels, these data could not be taken simultaneously, but stem from a subsequent run after changing the readout combination of anode segments at the QDC.

5 Conclusions

At a future e^+e^- linear collider, Compton polarimeters will be employed to measure the beam polarisation to a precision of $\delta\mathcal{P}/\mathcal{P} = 0.25\%$, using Cherenkov detectors to register the scattered Compton electrons.

A compact two channel prototype detector has been designed and constructed such that it will allow nearly all aspects of the final detector to be studied. In particular, it has been designed for easy exchange of the photodetectors and the calibration light source, but also the inter-channel wall could be exchanged in order to test different materials for a final detector.

The prototype has been operated successfully in a first testbeam campaign using four different photodetectors. The dynamic range of the detector and the pedestal stability fulfill the ILC requirements. The measurements have been compared to a detailed simulation of the prototype and several alignment methods have been tested.

In particular, a method to extract intra-channel beam position information has been developed, which could possibly allow to calibrate the Compton edge position without need for dedicated beam-time. Furthermore, the detector response has been studied as a function of the beam position. This will lead to a determination of each channel's response function which is important in order to control systematic effects on the final polarisation measurements.

In the future it is planned to use this prototype to compare different photodetectors and wall materials as well as to establish a calibration to the permille level as required for the ILC.

Acknowledgements

We thank C. Hagner and R. Klanner of the Institut für Experimentalphysik of the University of Hamburg for their support, and especially the design and technical construction team, B. Frensch and J. Pelz, as well as the head of the mechanical workshop, S. Fleig, and his entire team for their competent work.

The authors are grateful to W. Hillert, F. Frommberger and the entire ELSA team for their support during the testbeam period, for realising special beam requests and for many helpful discussions concerning a multitude of different ELSA technicalities. Further thanks go to K. Desch, J. Kaminski, D. Elsner, and many others for help and support with the planning and setup before, during, and after the two weeks in Bonn.

The authors acknowledge the financial support of the Deutsche Forschungsgemeinschaft in the DFG project Li 1560/1-1 as well as the complementary support by the Initiative and Networking Fund of the Helmholtz Association, contract HA-101 ("Physics at the Terascale").

References

- [1] The ILC Collaboration, “*ILC Reference Design Report, Volumes 1-4*”
 “1: *Executive Summary*,” J. Brau, Y. Okada, N. Walker (eds.) [arXiv:0712.1950 physics.acc-ph];
 “2: *Physics at the ILC*,” A. Djouadi, J. Lykken, K. Mönig, Y. Okada, M. Oreglia, S. Yamashita
 (eds.) [arXiv:0709.1893 hep-ph];
 “3: *Accelerator*,” N. Phinney, N. Toge, N. Walker (eds.) [arXiv:0712.2361 physics.acc-ph];
 “4: *Detectors*,” T. Behnke, C. Damerell, J. Jaros, A. Miyamoto (eds.) [arXiv:0712.2356 physics.ins-
 det].
- [2] G.A. Moortgat-Pick *et al.*, Phys. Rept. **460** (2008) 131, [arXiv:hep-ph/0507011].
- [3] I. Marchesini, “Triple Gauge Couplings and Polarization at the ILC and Leakage in a Highly Granular Calorimeter” Ph.D. Thesis, University of Hamburg, Hamburg, Germany, 2011.
- [4] The ALEPH, DELPHI, L3, OPAL and SLD Collaborations, the LEP and SLD Electroweak Working Groups and the SLD Heavy Flavour Group, Phys. Rept. **427** (2006) 257; [arXiv:hep-ex/0509008].
- [5] S. Boogert *et al.*, JINST **4** (2009) P10015. [arXiv:0904.0122v2 physics.ins-det].
- [6] V. Gharibyan, N. Meyners, and K.P. Schüller, TESLA Report 2001-23, Part III, LC-DET-2001-047, DESY, February 2001; DESY 2001-011, March 2001
- [7] E. Fokitis *et al.*, Nucl. Phys. Proc. Suppl. **44** (1995) 246,
- [8] A. Bideau-Mehu *et al.*, J. Quant. Spectrosc. Radiat. Transf. **25** (1981), 395.
- [9] R.D. Elia, “*Measurement of the left-right asymmetry in Z boson production by electron-positron collisions*,” SLAC-0429,
 R.C. King, “*A precise measurement of the left-right asymmetry of Z boson production at the SLAC linear collider*,” SLAC-0452.
- [10] The GEANT4 Collaboration, Nucl. Instrum. Meth. A **506**, Issue 3 (2003), 250-303;
 The GEANT4 Collaboration, IEEE Trans. Nucl. Science 53 No. 1 (2006), 270-278; ISSN: 0018-9499
- [11] The GEANT4 Collaboration, “*GEANT4 – Physics Reference Manual*,”
[http://geant4.web.cern.ch/geant4/UserDocumentation/UsersGuides/PhysicsReference ...](http://geant4.web.cern.ch/geant4/UserDocumentation/UsersGuides/PhysicsReferenceManual/fo/PhysicsReferenceManual.pdf)
 Manual/fo/PhysicsReferenceManual.pdf (cont’d)
- [12] E. Albrecht *et al.*, “*VUV Absorbing Vapours in n-Perfluorocarbons*,” CERN-EP/2002-099.
- [13] HAMAMATSU PHOTONICS K.K. (<http://sales.hamamatsu.com/> abbrev. as ~hamamatsu/
 R7600U-03-M4 (2007): ~hamamatsu/assets/pdf/parts_R/R5900U_R7600U_TPMH1291E03.pdf
 R7600-00-M64 (2006): ~hamamatsu/index.php?id=13195917
 R7400U-06(03) (2004): ~hamamatsu/assets/pdf/parts_R/R7400U_TPMH1204E07.pdf
- [14] PerkinElmer, Lambda 800 Spectrometer
<http://las.perkinelmer.com/Catalog/default.htm?CategoryID=Lambda+800+Spectrometer>
- [15] John E. Hatch (Ed.), “*Aluminum: Properties and Physical Metallurgy*,” American Society for Metals, Metals Park, Ohio, USA, 1984.
- [16] Agilent Technologies, LED of type: HLMP-CB30-NRG00
 Datasheet: <http://www.chipcatalog.com/Agilent/HLMP-CB30-NRG00.htm>
- [17] W. Hillert, Eur. Phys. J. A **28S1** (2006) 139.
- [18] PHOTONIS USA
 XP1911/UV (1999): <http://www.photonis.com/upload/industryscience/pdf/pmt/XP1911UV.pdf>

wavelength	R_{diam}	R_{roll}
160 nm	74 %	11 %
180 nm	77 %	18 %
200 nm	81 %	27 %
220 nm	84 %	30 %
240 nm	86 %	37 %
500 nm	85 %	40 %
520 nm	84 %	39 %
650 nm	83 %	40 %
900 nm	82 %	39 %

Table 1: The reflectivities of diamond-milled quality aluminium R_{diam} and of rolled quality aluminium R_{roll} as determined with the PERKINELMER spectrometer and implemented in the GEANT4 simulation. For the rolled aluminium, only the wavelength dependency is transferred to the simulation, while the absolute normalisation is adjusted to prototype data.

photodetector types	sensitive area in [mm ²]	wavelength range [nm]	typical gain	response time	anode pads
R7600U-03-M4 ^(a)	18.0×18.0	185 - 600	$1.8 \cdot 10^6$	11.0 ns	4
R7600-00-M64 ^(a)	18.1×18.1	300 - 600	$0.3 \cdot 10^6$	13.4 ns	64
R7400U-06(03) ^(a)	$\varnothing = 8 \text{ mm}$	160(185) - 600	$0.7 \cdot 10^6$	6.5 ns	1
XP1911/UV ^(b)	$\varnothing = 15 \text{ mm}$	200 - 600	$0.9 \cdot 10^6$	28.0 ns	1

Photodetector from: (a) HAMAMATSU, (b) PHOTONIS.

Table 2: Key characteristics of the four different photomultipliers from HAMAMATSU and PHOTONIS [13, 18]. The two MAPMs (R7600U-03-M4 and R7600-00-M64) have a quadratic cross-section of similar size, but differ in the number of anodes and in their wavelength range. The two SAPMs (R7400U-03 and R7400U-06) differ in the size of their sensitive areas and slightly in wavelength range.

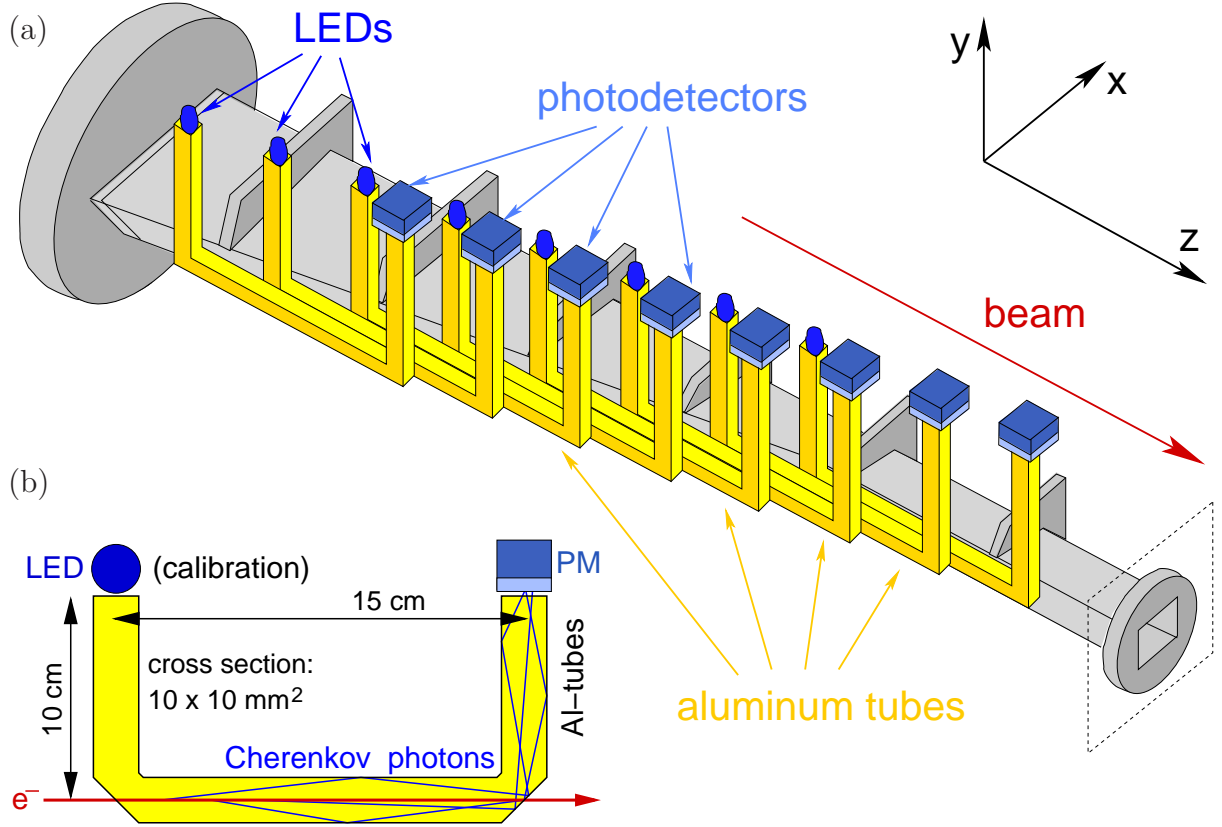
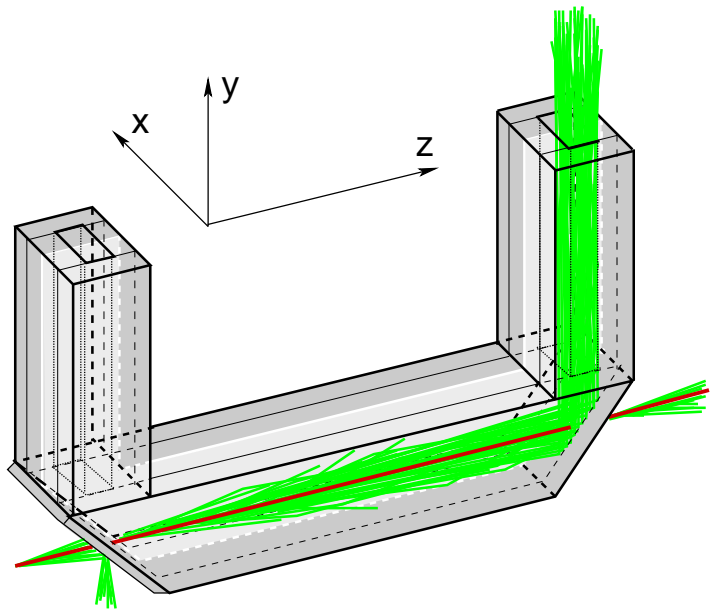


Figure 1: (a) Illustration of a Cherenkov detector for ILC polarimetry, here for better visibility with eight instead of the actually foreseen 20 readout channels; and (b) sketch of one such gas-filled aluminium channel.

Figure 2: Event display of the 2-channel prototype simulation:
The electron beam (red) passes from left to right through the U-base of the aluminium tubes filled with perfluorobutane, C_4F_{10} , and emits Cherenkov photons (green). These are reflected upwards to a photodetector mounted on the hind U-leg. The channels are separated by a thin foil (light grey).
Due to a surrounding gas-filled box (not shown), Cherenkov radiation can also be emitted before/after the electron beam enters/exits the aluminium tubes, but it cannot reach the photodetector.



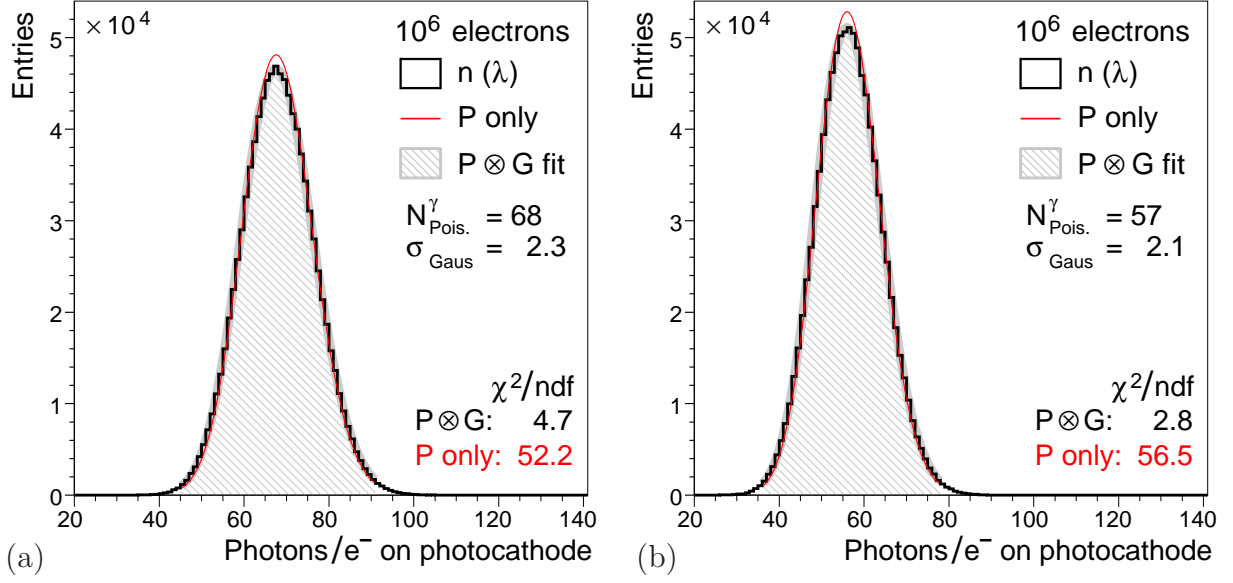


Figure 3: Average number of photons reaching the photocathode per 2 GeV electron: (a) with equal reflectivities for all channel walls and (b) with a reduced reflectivity of the inter-channel wall ($r = 50\%$).

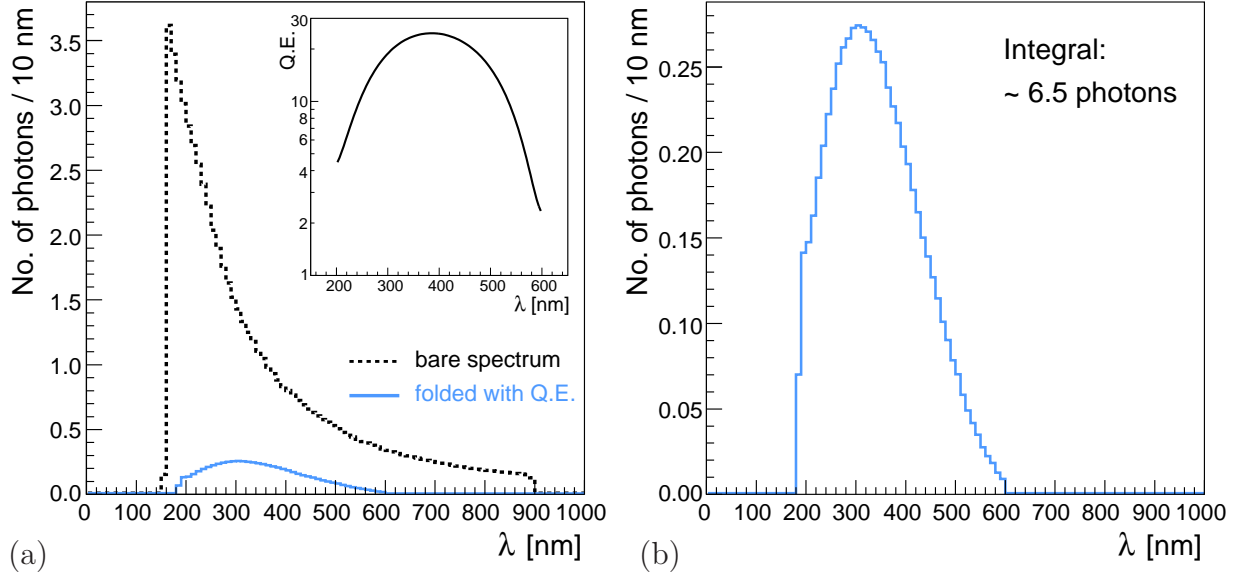


Figure 4: Cherenkov spectra: (a) at the photocathode (dotted line) and (b) convoluted with the quantum efficiency (Q.E.) of the 2×2 MAPM (R7600U-03-M4), see the insert in (a). The convoluted spectrum is also superimposed in (a) as the solid line.

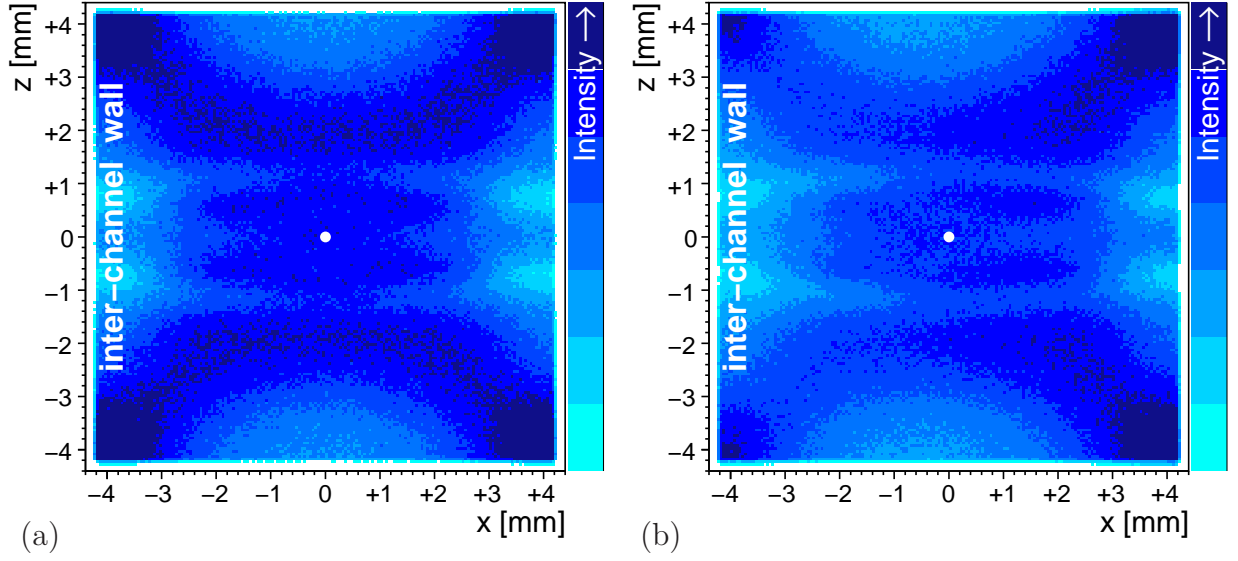
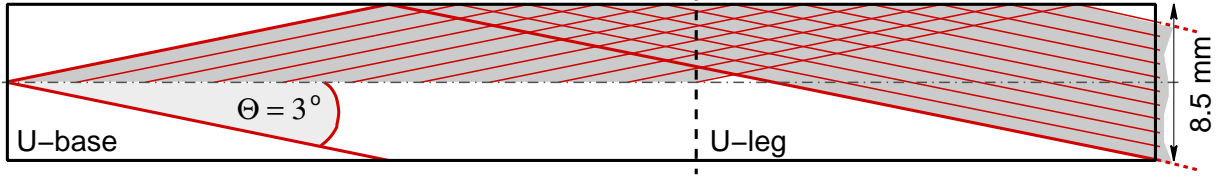


Figure 5: Light distribution on the photocathode: (a) with equal reflectivities for all channel walls, (b) with a reduced reflectivity for the inter-channel wall at $x = -4.25$ mm. The white dot indicates the channel centre; the intensity scale ranges from 40% to 100%.

(a) photons emitted in the horizontal/vertical plane



(b) photons emitted toward the channel corners

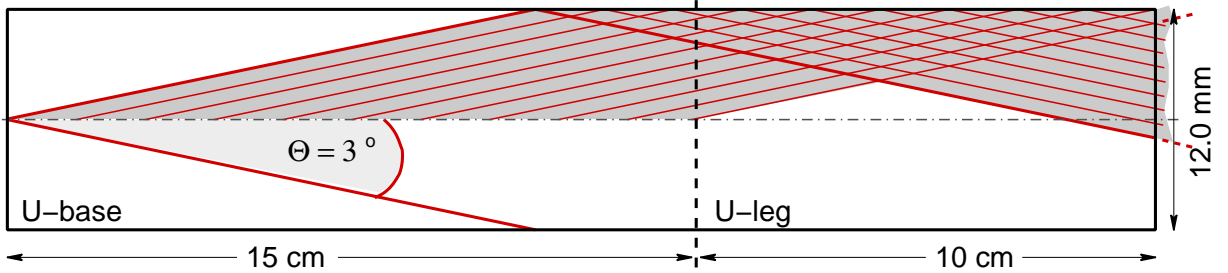


Figure 6: Sketches of possible light paths for electrons traversing the channel along the central axis and the Cherenkov angle of the chosen gas ($\Theta_{\text{Ch}} = 3^\circ$). The channel aspect ratio has been enlarged by a factor of 4 for better visibility.

(a) Photons emitted in the horizontal/vertical plane illuminate the entire channel width at the photocathode, while (b) photons emitted towards the channel corners only illuminate half the channel width. The 90° reflection at the end of the U-base (indicated by the vertical dashed line) has no influence on the symmetry of the distribution.

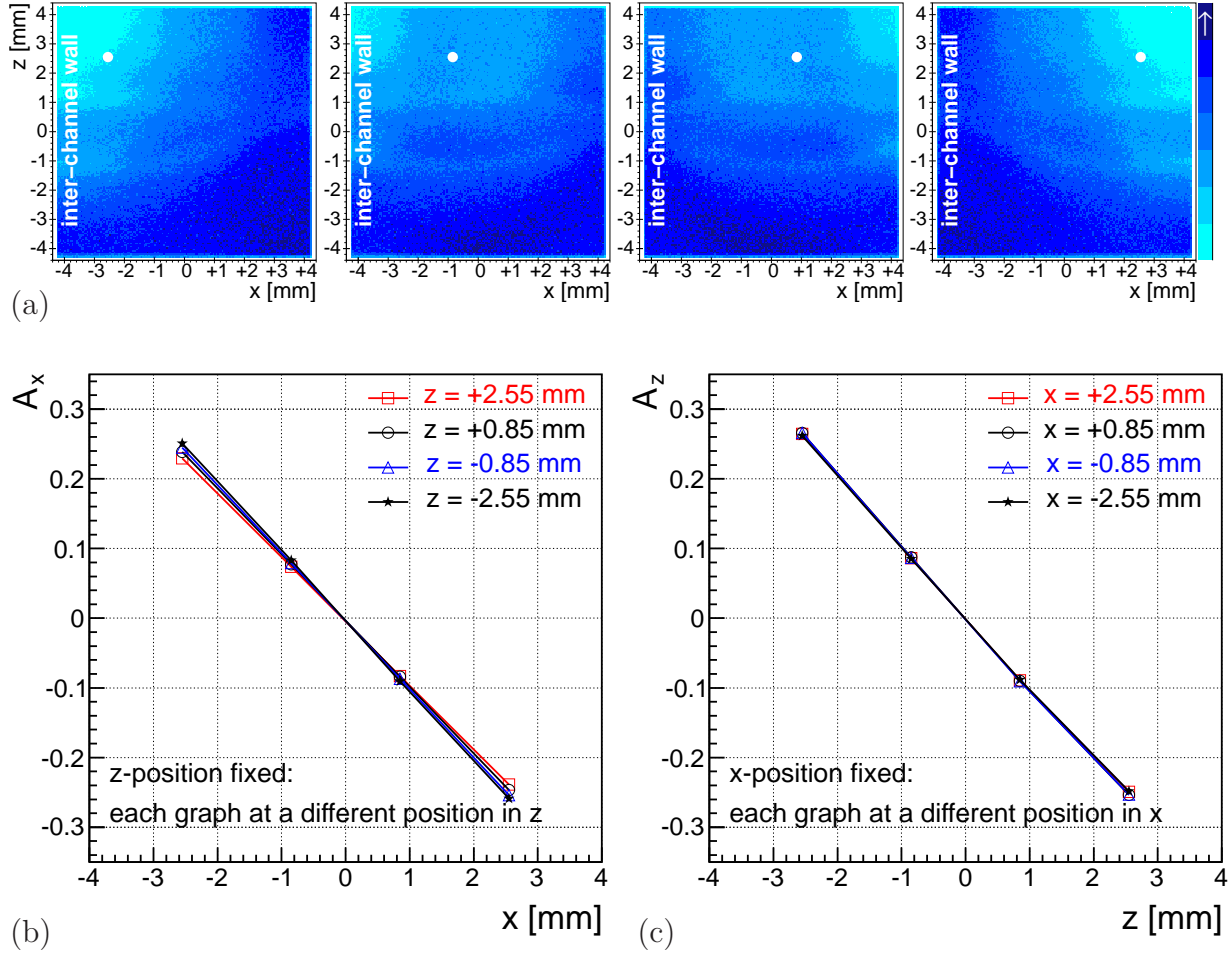


Figure 7: (a) Simulated light yield at the photocathode for a horizontal beam position scan at $y = +2.55$ mm and equal reflectivities for all channel walls. The asymmetries have been calculated respectively from horizontal and vertical scans using 10^5 electrons for each beam position: (b) A_x asymmetry for different z -positions and (c) A_z asymmetry for different x -positions. The beam y -position translates directly to the z -position in the readout plane (white dots).

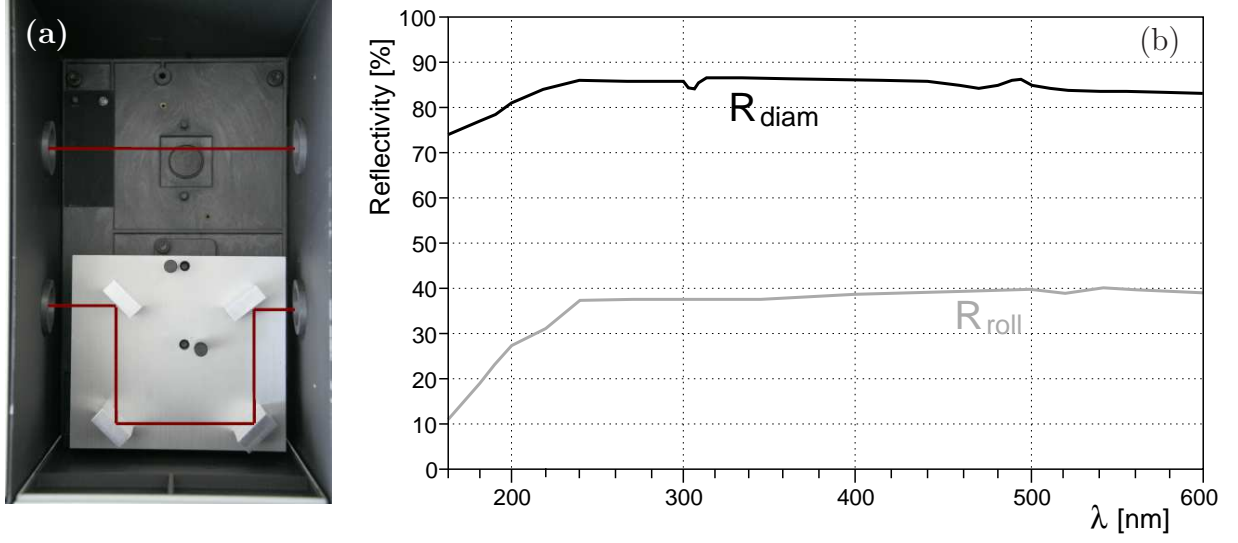


Figure 8: (a) Photograph of the interior of the modified PERKINELMER transmission spectrometer with the indicated paths of the reference beam (top) and the measurement beam (bottom). (b) Measured reflectivities of diamond-milled aluminium (upper line) and of rolled aluminium (lower line).

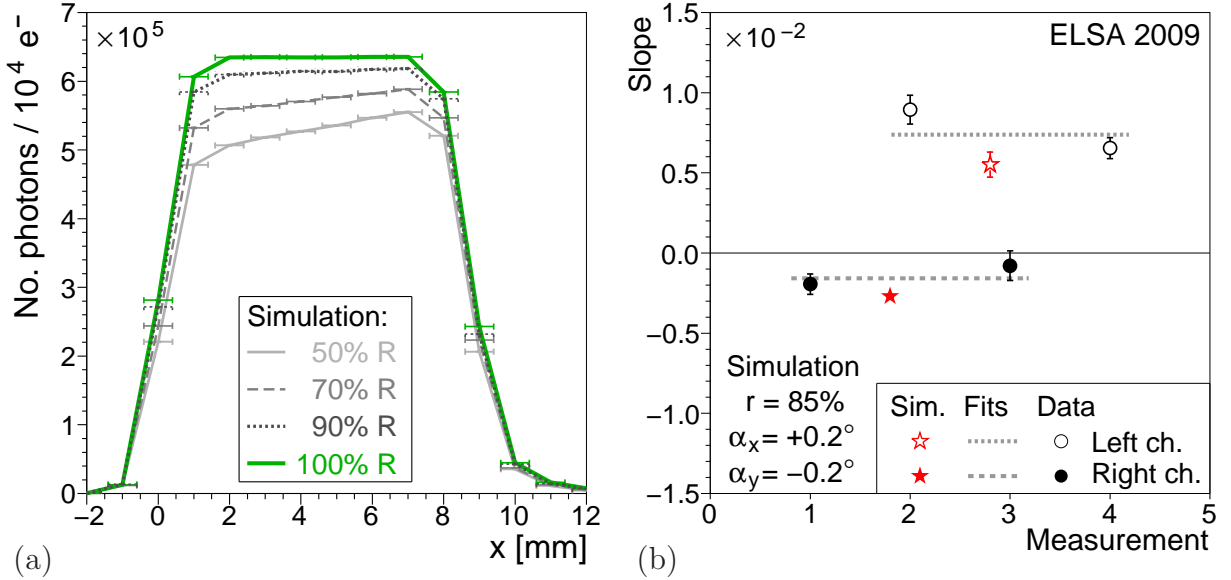


Figure 9: (a) Simulations with different percentages of the inter-channel wall reflectivity w.r.t. to the other walls' reflectivities lead to different plateau shapes. (b) A comparison with data allows to determine the inter-channel wall reflectivity to be $R_{\text{roll}} = (85\% \pm 2\%) \cdot R_{\text{diam}}$ under glancing angle.

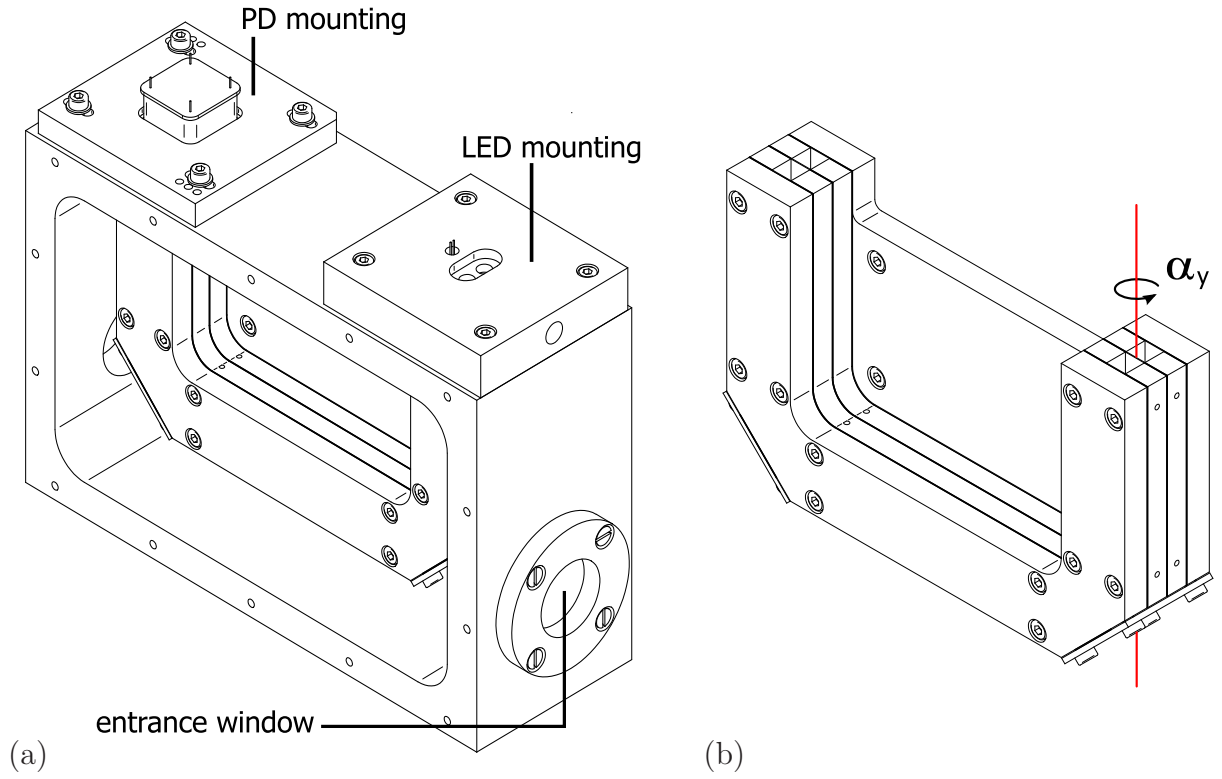


Figure 10: Parts of a technical drawing for the assembly of the prototype: (a) the box base body, already including the channel structure (b) of two parallel U-shaped channels.

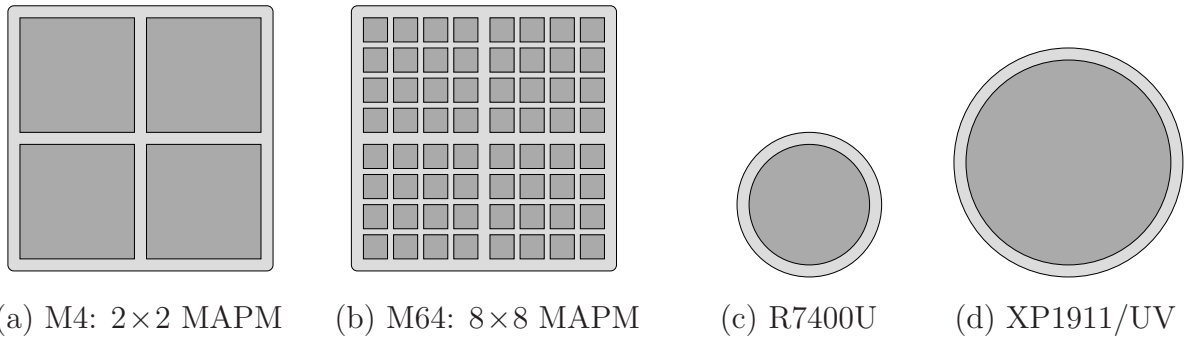
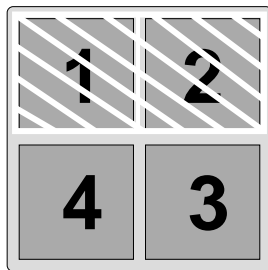
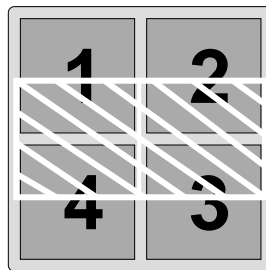


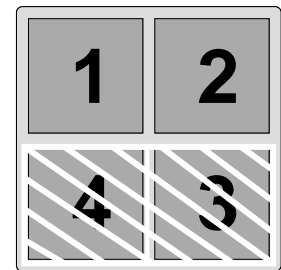
Figure 11: Anode schemes of the different multi- and single-anode photomultiplier types, in correct relative scaling.



(a) upper position



(b) middle position



(c) lower position

Figure 12: Different positions of the MAPMs (grey) on the detector channels (hatched).



Figure 13: Calibration LEDs covered by POM tubes.

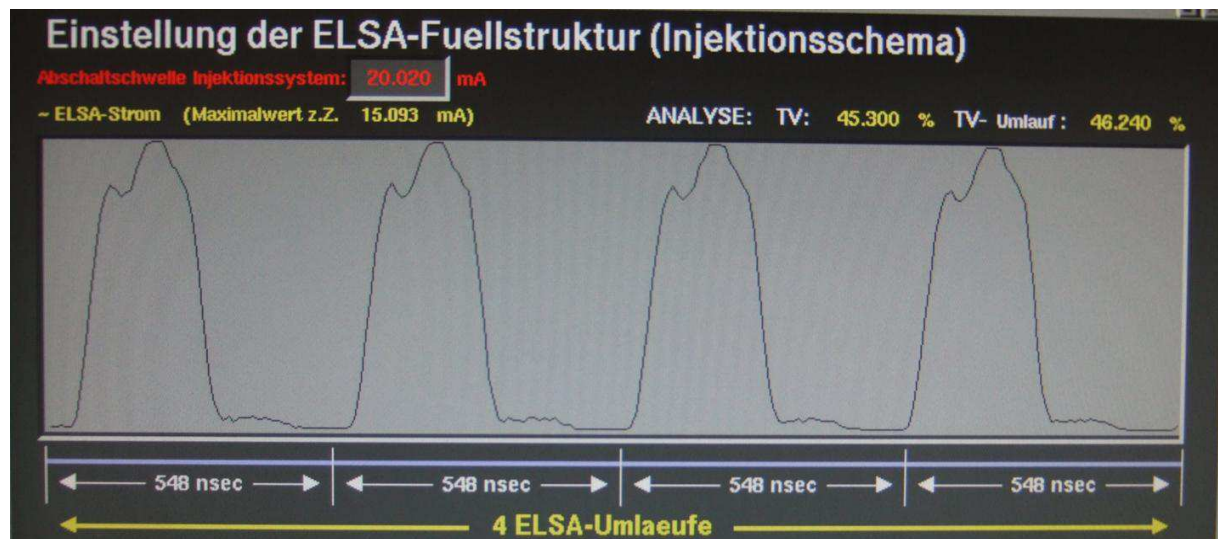


Figure 14: Example of a typical ELSA fill structure for four revolutions of 548 ns. About half of the available buckets are filled.

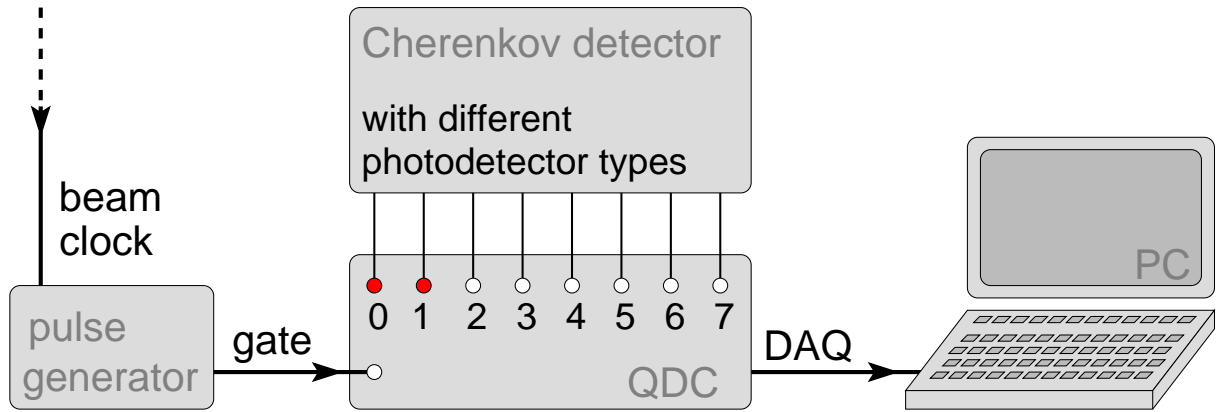


Figure 15: Block diagram of the readout chain as realised during the testbeam period.

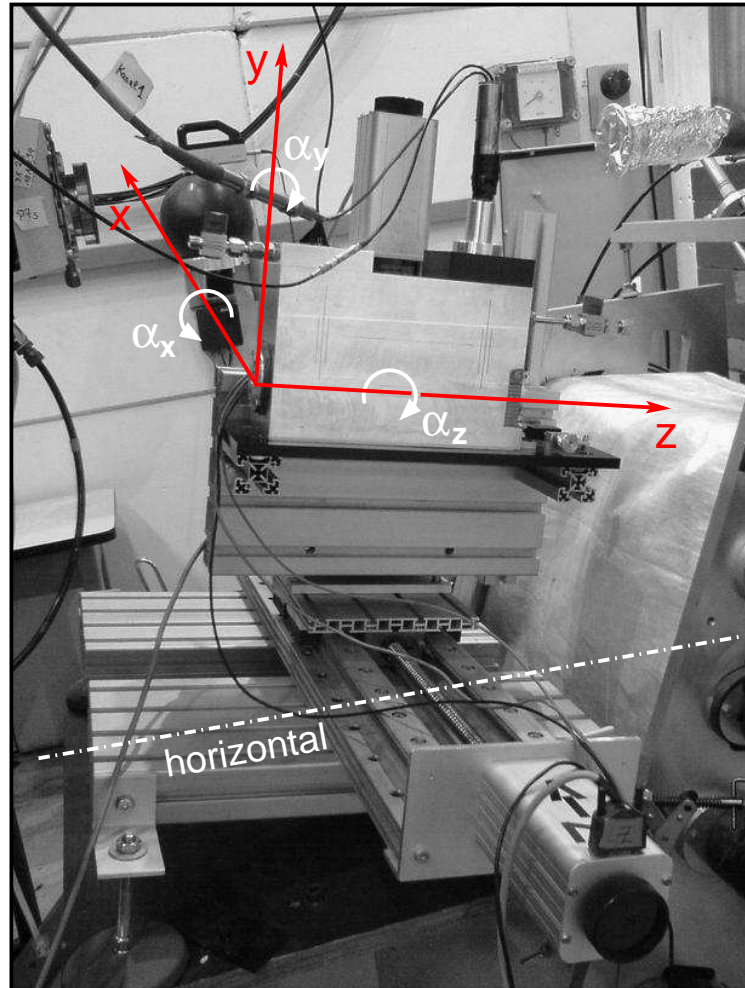


Figure 16: The prototype Cherenkov detector on its base plate (black, with the rotational mechanism visible on the right) is mounted on a stage moveable along the x- and y-axis.

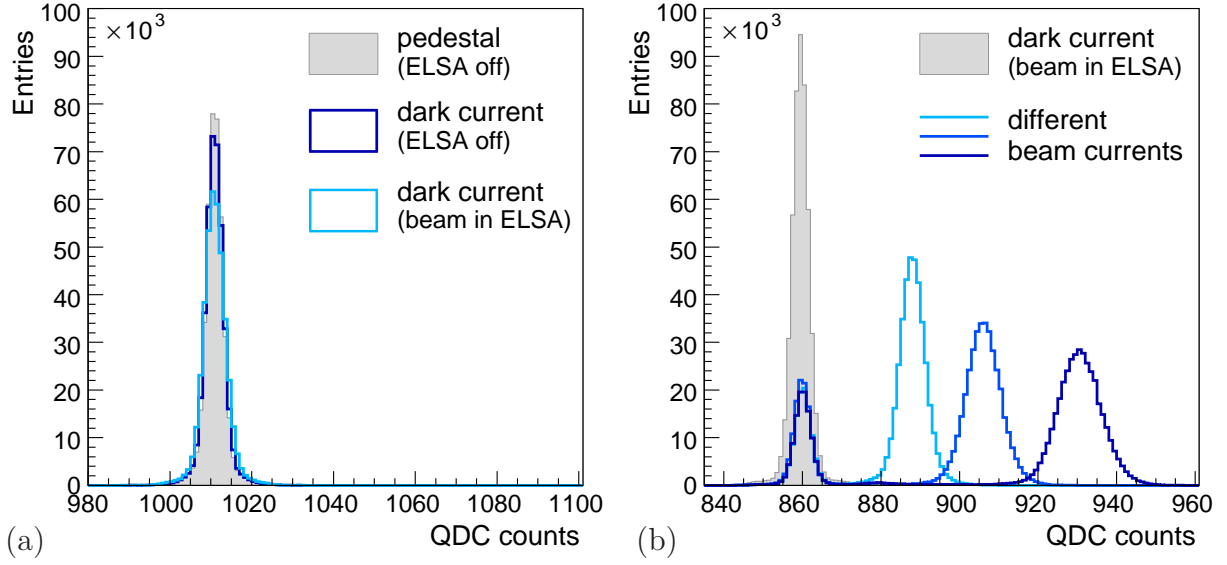


Figure 17: Data recorded with the 2×2 MAPM (R7600U-03-M4):
 (a) QDC response without bias voltage applied to the photodetector (pedestal) and with 400 V applied (dark current), both without and with beam circulating in ELSA.
 (b) Cherenkov signals increase with increasing electron beam current, while the pedestal position remains stable. The 4:1 area ratio between the beam signal peak and the pedestal of each open histogram corresponds to the beam extraction cycle of 4s:1s.

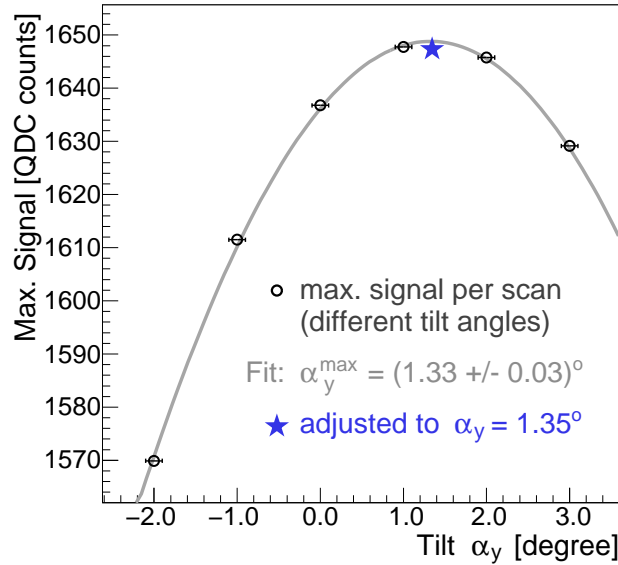


Figure 18: Detector alignment with the 2×2 MAPM (bias voltage 860 V): The tilt in the (x, z) -plane is determined from x -scans for six different tilt angles. An additional measurement for the adjusted tilt of $\alpha_y = 1.35^\circ$ is also displayed.

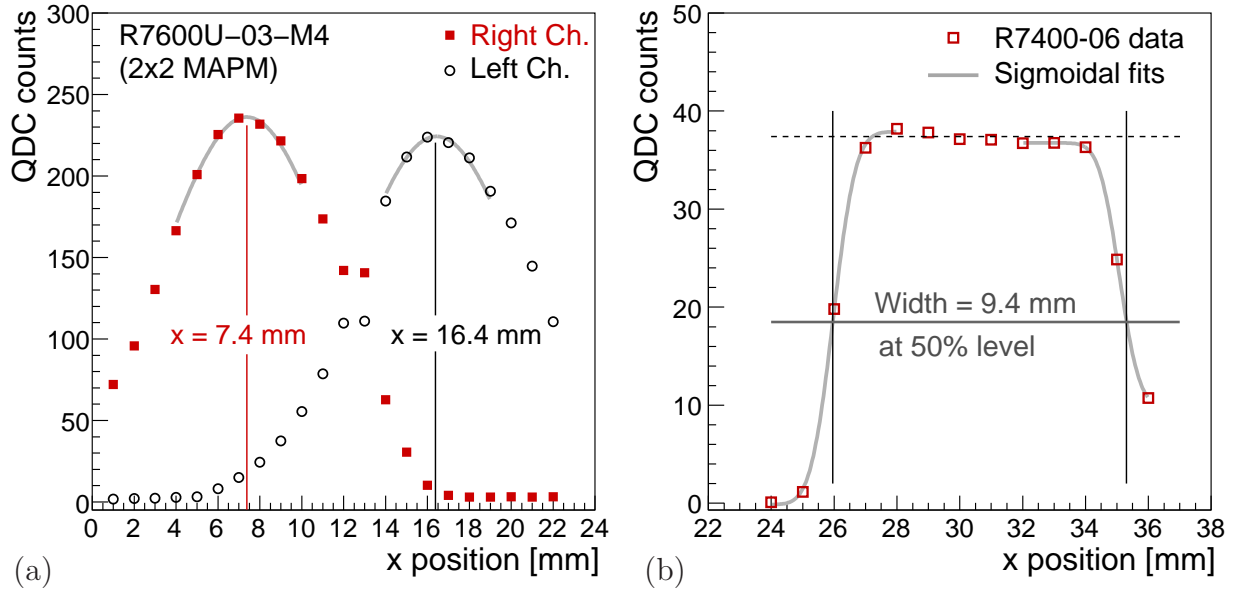
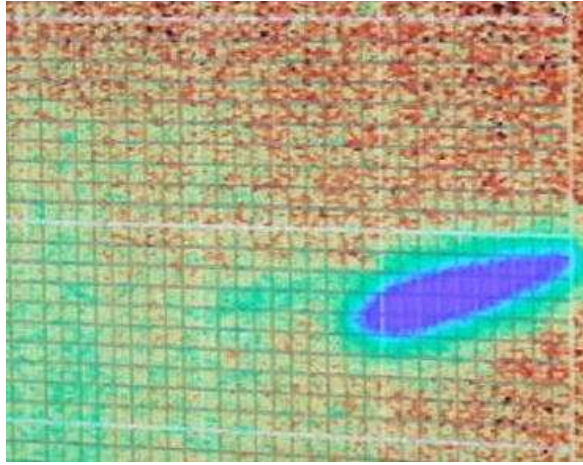
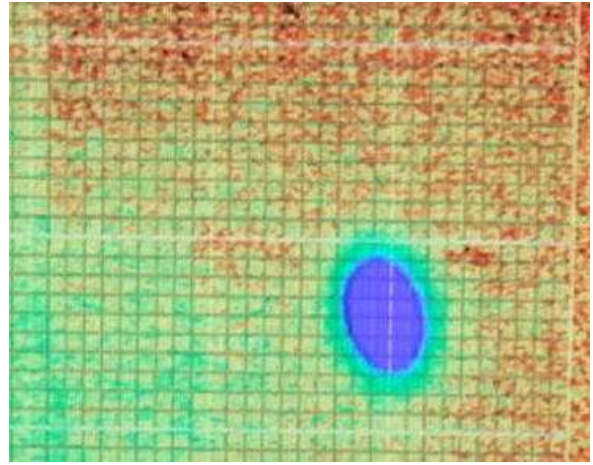


Figure 19: Results from x -scans for two different types of photomultipliers: (a) the 2×2 MAPM (R7600U-03-M4, bias voltage 860 V), (b) the SAPM (R7400U-06, bias voltage 300 V). The absolute x -values correspond to different stage zero-positions; only the relative values are relevant.



(a) larger, elongated beam spot



(b) smaller, nearly round beam spot

Figure 20: Two beam spot shapes observed at ELSA when (a) the data in Fig. 19(a) and (b) the data in Fig. 19(b) were recorded. The dimensions of the spots are approximately 4×2 mm for the elongated shape in (a) and 1.5×2 mm for the rounder shape in (b).

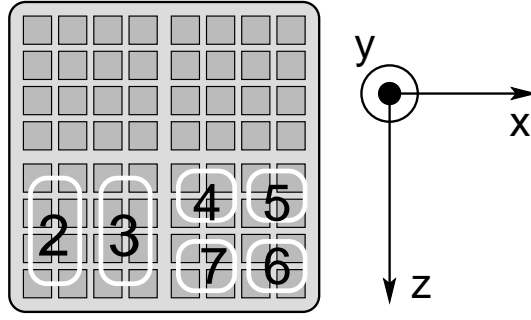


Figure 21: Readout configuration for the 8×8 MAPM: The anode pads are depicted as grey squares; the readout channels as numbered white rectangles.

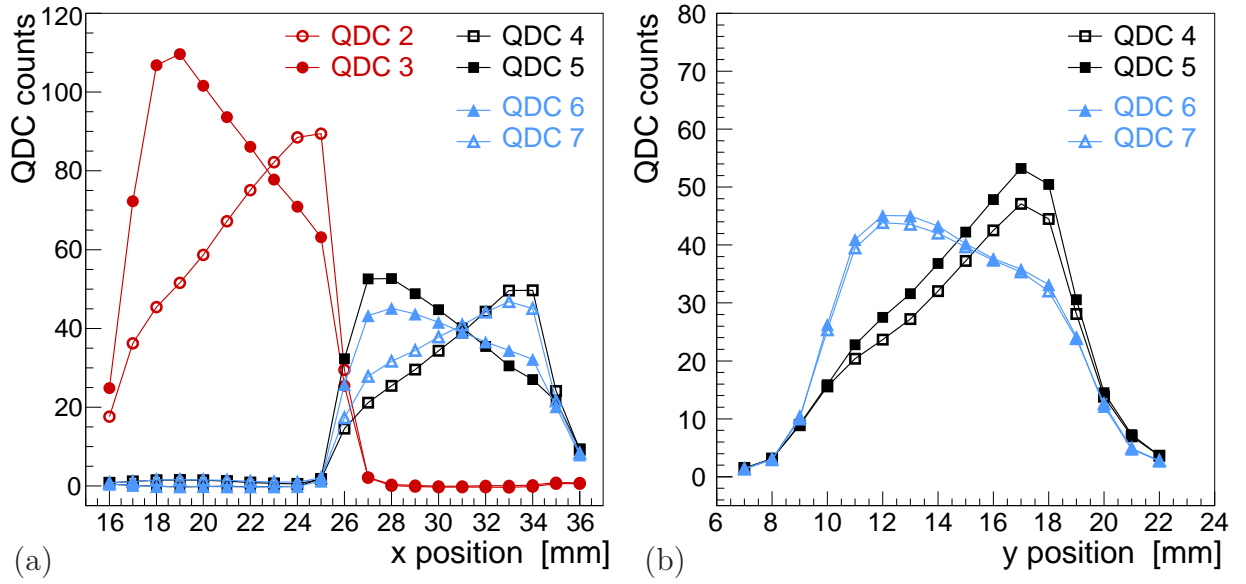


Figure 22: Beam position scan data recorded with the 8×8 MAPM (bias voltage 500 V): (a) x-scan across both channels and (b) y-scan on the left channel.

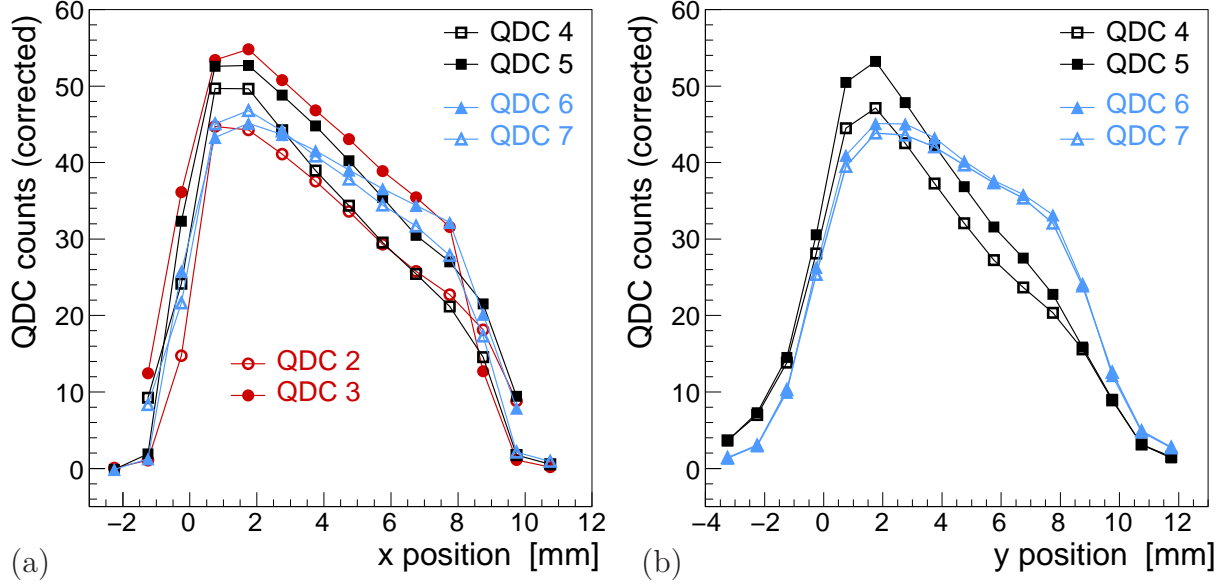


Figure 23: Different visualisation of the position scan data presented in Figure 22 with the emphasis on shape and amplitude differences: (a) x-scan data and (b) y-scan data.

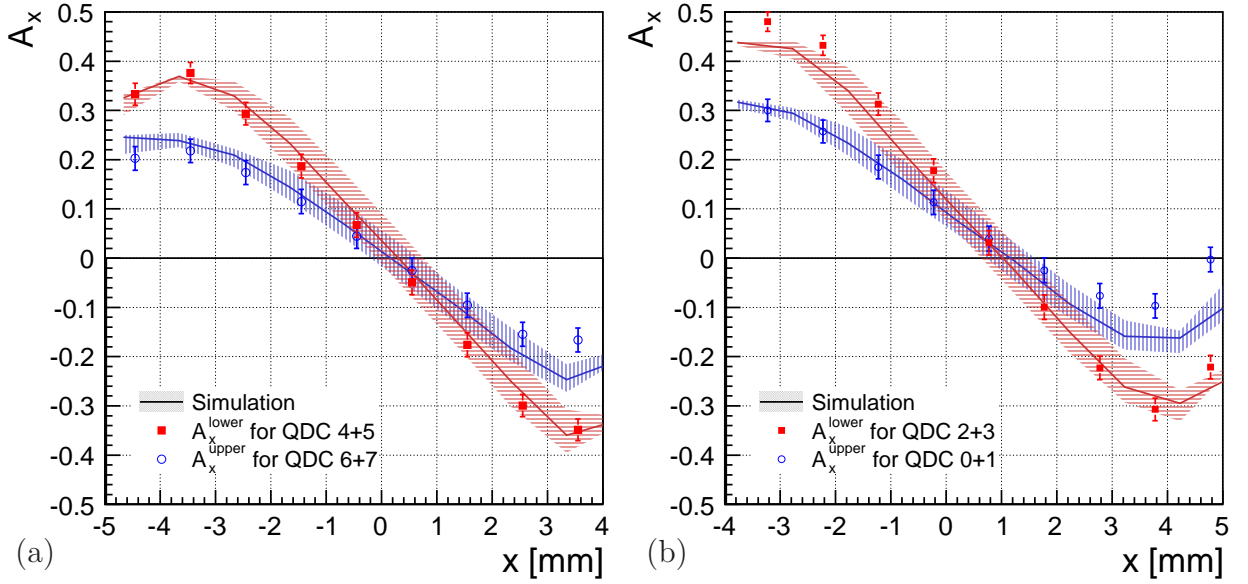


Figure 24: Asymmetries calculated from the position scan data sets recorded with the 8×8 MAPM. (a) A_x for QDC-pairings 4+5 and 6+7 on the left detector channel from the same data as used in Fig 23 (b) A_x on the right detector channel from a subsequent run. In addition simulated asymmetries for $\alpha_x = 0.2^\circ$ and $\alpha_y = -0.2^\circ$ are shown for both channels. The error bands correspond to a variation of α_y by $\pm 0.1^\circ$.